A numerical investigation of the flow around a motorbike when subjected to crosswinds

Fintelman, Danielle; Hemida, Hassan; Sterling, Mark; Li, Francois-Xavier

DOI:
10.1080/19942060.2015.1071524

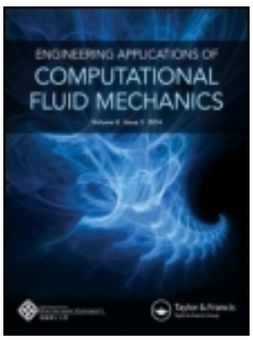

Taylor & Francis
Taylor & Francis Group

Engineering Applications of Computational Fluid Mechanics

ISSN: 1994-2060 (Print) 1997-003X (Online) Journal homepage: http://www.tandfonline.com/loi/tcfm20

A numerical investigation of the flow around a motorbike when subjected to crosswinds

D. Fintelman, H. Hemida, M. Sterling & F-X. Li

To cite this article: D. Fintelman, H. Hemida, M. Sterling & F-X. Li (2015) A numerical investigation of the flow around a motorbike when subjected to crosswinds, Engineering Applications of Computational Fluid Mechanics, 9:1, 528-542, DOI: 10.1080/19942060.2015.1071524

To link to this article: http://dx.doi.org/10.1080/19942060.2015.1071524

Published online: 11 Sep 2015.

Engineering Applications of Computational Fluid Mechanics, 2015
Vol. 9, No. 1, 528–542, http://dx.doi.org/10.1080/19942060.2015.1071524

Taylor & Francis
Taylor & Francis Group

A numerical investigation of the flow around a motorbike when subjected to crosswinds

D. Fintelman[a*], H. Hemida[b], M. Sterling[b] and F-X. Li[a]

[a]*School of Sport, Exercise and Rehabilitation Sciences, University of Birmingham, UK;* [b]*School of Civil Engineering, University of Birmingham, UK*

(*Received 3 April 2013; final version received 25 June 2015*)

Crosswinds have the potential to influence the stability and therefore the safety of a motorbike rider. Numerical computations using both delayed detached-eddy simulations (DDES) and Reynolds-Averaged Navier-Stokes (RANS) were employed to investigate the flow around a motorbike subjected to crosswinds with yaw angles of 15, 30, 60 and 90 degrees. The Reynolds number was 2.2 million, based on the crosswind velocity and the height of the rider from the ground. The aerodynamic force coefficients and flow structures around the motorbike and rider were obtained and analysed. Although both DDES and RANS provided comparable overall aerodynamic forces, RANS failed to predict both the DDES surface pressures at the separation regions and the location and size of the main circulation region. The DDES results showed that the drag coefficients decrease with increasing yaw angles, while the side force coefficients significantly increase. It was found that increasing yaw angles result in stronger vortex shedding around the windshield and helmet.

Keywords: motorbike; crosswind; DDES; RANS; aerodynamic forces; flow structures

1. Introduction

There are an estimated 200 million motorbikes around the world (Shuhei, 2006). The motorbike and rider experience different aerodynamic forces and moments when travelling along roads. Scibor-Rylski and Sykes (1984) state that improving the aerodynamic performance of a rider is an important factor in reducing fuel consumption and improving motorbike maneuverability. In addition, crosswinds have the potential to severely influence the stability of the motorbike and rider, due to increased aerodynamic forces (Cheli, Bocciolone, Pezzola, & Leo, 2006). These forces include side forces, rolling, pitching, and yawing moments, in addition to the normal aerodynamic drag and lift forces. Despite the several reported fatal accidents due to the effects of crosswinds, aerodynamic research relating to crosswinds is rather limited (Carr, 2011; Donell, 2010; Gauger, 2013). In contrast, crosswind research on other road vehicles (e.g., cars and lorries) is common (Baker et al., 2009; Cheli, Belforte, Melzi, Sabbioni, & Tomasini, 2006; Guilmineau & Chometon, 2009; Hemida & Baker, 2010; Hemida & Krajnović, 2009a; Sterling et al., 2010; Tsubokura et al., 2010; Wang, Xu, Zhu, Cao, & Li, 2013; Wang, Xu, Zhu, & Li, 2014). Given the importance of motorbikes as a form of transport, further research is required in order to ensure that traffic regulations and ultimately the safety of the road network is as robust as possible.

Researchers have used wind tunnel experiments to investigate and optimize the stability and aerodynamic performance of motorbikes and many of their individual components. For example, the effect of handlebar fairing and windshield on the stability of a full-scale motorbike was investigated by Cooper (1983), while Bridges and Russell (1987) studied the effect of a 'topbox' on the stability of a motorbike. In the paper of Araki and Gotou (2001), the aerodynamic characteristics of different motorbikes were compared and an outline of the aerodynamic development of motorbikes by means of wind tunnels presented. Whereas the three aforementioned studies focused on aerodynamic performance and stability, limited data is available on the forces experienced by motorbikes in crosswinds. Ubertini and Desideri (2002) experimentally measured the aerodynamic forces and moments on a scooter and rider at different yaw angles up to 10° (with the yaw angle defined as the angle the crosswind makes relative to the direction of travel). It was observed that the aerodynamic drag force coefficients increased by approximately 16% as a result of the increasing yaw angle. The side forces and yawing moments tended to increase linearly with the yaw angle. Although this research provided an insight into the aerodynamic effects (albeit over a reduced range of yaw angles), due to the nature of the experiments, no information pertaining to the instantaneous flow structures and pressure distributions were obtained.

*Corresponding author. Email: DMF144@bham.ac.uk

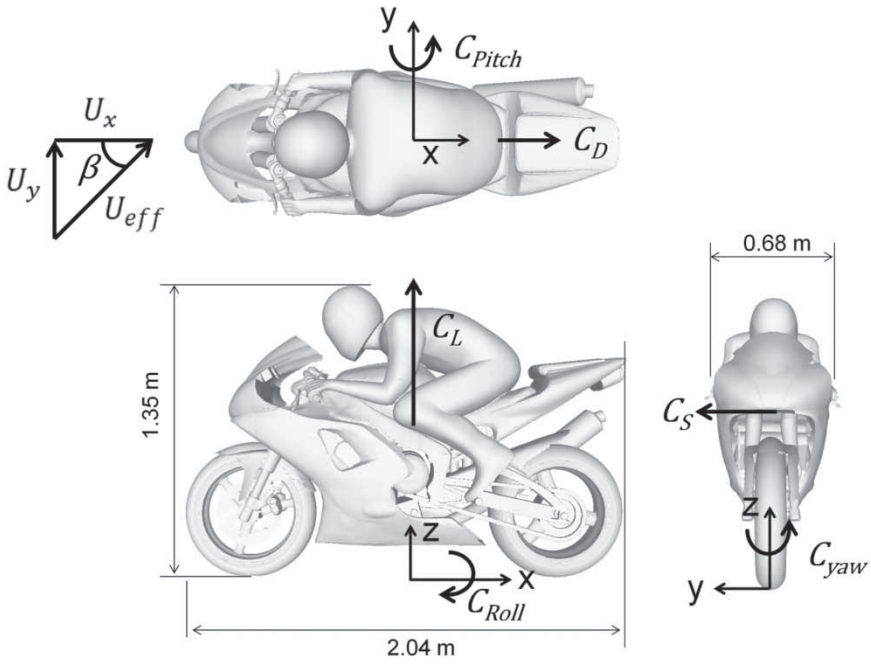

Figure 1. Orthogonal views of the motorbike showing the aerodynamic forces and moments, velocity directions and yaw angle, β (the angle between the motorbike traveling direction, U_x, and the effective crosswind, U_{eff}).

Computational fluid dynamics (CFD) already plays a significant role in motorbike design (Angeletti, Sclafani, Bella, & Ubertini, 2003). For example, it has been used to investigate the three-dimensional flow characteristics inside motorbike engines, which is relatively difficult and rather expensive to obtain experimentally (Chu, Chang, Hsu, Chien, & Liu, 2008; Gentilli, Zanforlin, & Frigo, 2006). Furthermore, CFD has been used to optimize individual engineering components, to improve energy efficiency and to determine the effect of local geometry changes of the motorbike on the aerodynamic forces (Takahashi et al., 2009; Watanabe, Okubo, Iwasa, & Aoki, 2003). Sakagawa, Yoshitake, and Ihara (2005) investigated the airflow pattern around a motorbike with the standard k-ε Reynolds-Averaged Navier-Stokes (RANS) simulation for the no-crosswind case in order to optimize aerodynamic performance. In addition, they carried out simulations for the design of an engine cooling system. However, as the flow around a motorbike is fully turbulent, and thus varies in both time and space, the results obtained from the RANS simulations lack information about the instantaneous flow structures.

The aim of this study is to provide an improved understanding of the time-averaged and instantaneous flow around a motorbike subjected to crosswinds with different yaw angles using both delayed detached-eddy simulation (DDES) and RANS techniques. In the current work, the Reynolds number is 2.2×10^6, based on the effective crosswind velocity and the height of the rider from the ground. The open source CFD package OpenFOAM was used to solve the flow equations.

2. Motorbike model

The current research was carried out on a sportive Yamaha R1 motorbike with rider (see Figure 1). The Yamaha R1 is a popular motorbike which has been manufactured since 1998 (Yamaha, 2009). Figure 1 shows the geometry of the motorbike, including the nomenclature adopted in this current work. The coordinate system used in this paper is also shown, where x opposes the direction of travel, y is in the lateral direction and z is in the vertical direction. The resultant of the negative motorbike velocity (U_x) with the crosswind velocity (U_y), yields the effective crosswind velocity (U_{eff}), which acts at a yaw angle (β) relative to the motorbike's direction of travel. The length, height and width of the motorbike with rider are 2.04, 1.35 and 0.68 m, respectively. The motorbike model maintains a high level of geometrical detail including the main motorbike components, although small details such as cables and bolts are omitted.

3. Numerical method

The open source finite volume CFD package OpenFOAM (Version 2.1.1) was used to solve the incompressible flow equations in all the simulations of this paper. The flow around a motorbike subjected to crosswinds is dominated by highly three-dimensional turbulent flow structures. In order to obtain information about these turbulent structures in both time and space, time-dependent DDES based on Spalart-Allmaras modeling was used (Spalart et al., 2006). Although more computationally expensive than the RANS approach, DDES is more accurate and yields

information that is unobtainable from RANS. DDES is a hybrid technique that blends the RANS approach with the large eddy simulation (LES) approach. In the near wall region a RANS model is applied, while for the detached flow the LES approach is used. The two approaches are combined by means of a modified distance function

$$l_{\mathrm{DDES}} \equiv l - f_d \max(0, l - C_{\mathrm{DES}}\Delta) \quad (1)$$

where l is the distance from the wall, C_{DES} is an empirically-derived constant (0.65) and Δ is the largest dimension of the grid cell in all three directions, $\Delta = \max(\delta x, \delta y, \delta z)$. The function f_d is defined as

$$f_d \equiv 1 - \tanh([8r_d]^3) \quad (2)$$

$$r_d \equiv \frac{\nu_t + \nu}{\sqrt{U_{ij}U_{ij}}\kappa^2 l^2} \quad (3)$$

where ν_t is the kinematic eddy viscosity, ν is the kinematic viscosity, U_{ij} is the velocity gradient, κ is the Kármán constant and r_d is the ratio of the model length scale to the wall distance. In the region where $r_d \ll 1$ ($f_d = 1$), the LES model is employed.

The time derivatives were discretized using a second-order backward implicit scheme. The gradient and divergence terms were discretized using a second-order central differencing, except for the velocity divergence terms, for which the linear-upwind stabilized transport (LUST) scheme (a blend of 75% second-order linear scheme and 25% linear-upwind scheme) was used to optimize the balance between accuracy and stability. The transient 'pressure implicit with splitting of operator' (PISO) algorithm was implemented in the simulations to decouple the pressure and velocity (Issa, 1986).

In addition to DDES, a number of RANS computations have also been undertaken. The RANS simulations were performed using two turbulence models; the shear stress transport (SST) k-ω model (Menter, 1992) and the standard k-ε model (Launder & Spalding, 1974). The RANS equations predict the time-averaged velocity and pressure fields instead of calculating the complete flow pattern as a function of time. The SST k-ω predicts the turbulent viscosity by a relationship of the turbulent kinetic energy, k, and the specific dissipation ω near the wall, and the free-stream flow is solved for using a k-ε model. Separate transport equations are used for k and ω. On the other hand, the k-ε model uses a relation between the turbulent dissipation ε and turbulent kinetic energy to predict the turbulent viscosity.

4. Computational domain and boundary conditions

A generalized computational domain was used in this investigation (see Figure 2). Two inlet and two outlet boundaries are used to simulate the crosswind conditions. At the inlet boundaries, the flow has two components: one in the negative direction of travel, x, and one perpendicular to the direction of travel, y. The effective crosswind velocity was set constant at 25 m/s in all simulations. The lateral flow velocity, U_y, and the frontal flow, U_x, were dependent on the yaw angle of the crosswind and are expressed as:

$$U_x = \cos(\beta)U_{\mathrm{eff}}$$
$$U_y = \sin(\beta)U_{\mathrm{eff}}, \quad (4)$$

where β is the yaw angle. Four different yaw angles were investigated: 15°, 30° and 60° and 90°. The dimensions of the computational domain are shown in Figure 2, in which H is the height of the rider from the ground (1.35 m). The dimensions in the x-direction and z-direction were taken as constant for all simulations, while the dimension in the y-direction was extended for large yaw angles. The total y-dimension was set as 20 H for yaw angles between 15° and 30°, and 33 H for angles between 60° and 90°. These distances from the motorbike surface to the exit plane were chosen to be large enough for the zero-pressure exit boundary condition to be applied without affecting the flow or pressure fields around the motorbike. No-slip boundaries were applied on the surface of the motorbike, rider and

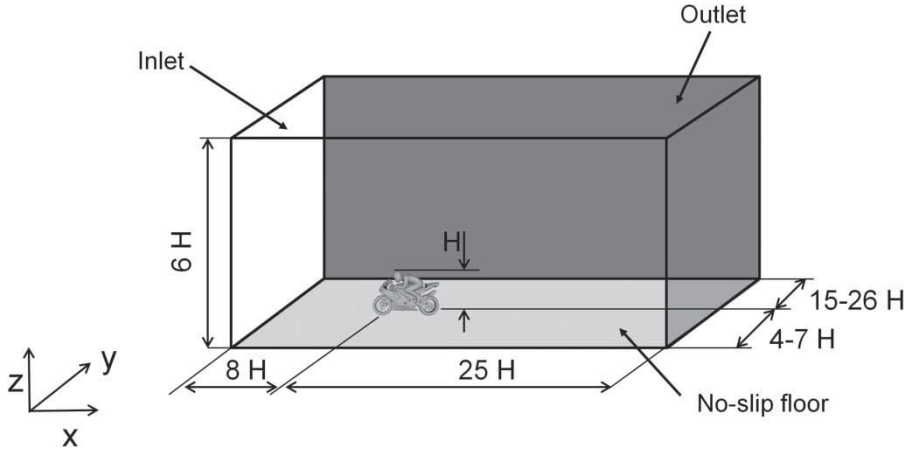

Figure 2. Computational domain dimensions.

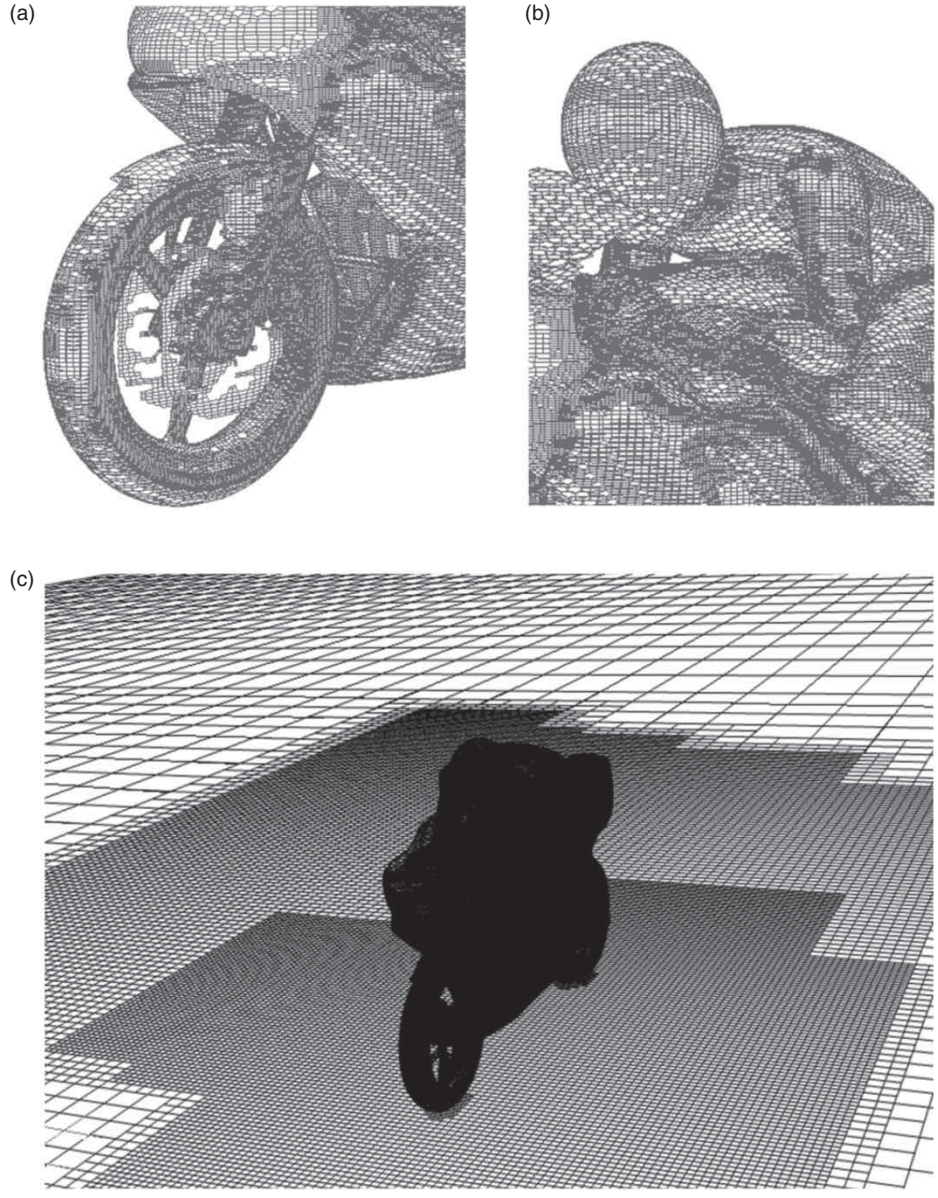

Figure 3. Coarse mesh around motorbike: (a) surface mesh wheel, (b) surface mesh rider, (c) ground mesh.

ground surface. The ground surface was simulated as a smooth wall with a velocity identical to the motorbike's speed ($U_x = 25\,\mathrm{m/s}$), representing correct relative movement between the motorbike and the ground. To give a tangential velocity similar to that of the ground for both wheels, they rotated with an angular velocity of 66.7 rad/s (front) and 64.5 rad/s (rear) in the simulations. The discrepancy in angular velocity between the wheels is a result of the different wheel diameters.

The surface mesh was created with OpenFOAM's SnappyHexMesh utility. The surface mesh contains 91% hexahedra-type cells, while the remaining 9% consist predominantly of polyhedral and prisms cells. Images of the surface mesh of the motorbike and rider are shown in Figures 3(a) and 3(b). To investigate the grid independency of the DDES simulations, two different meshes were evaluated: a coarse mesh and a fine mesh. The coarse mesh consisted of 3.8 million cells for the small yaw angles ranging from 15° to 30° and 4.0 million cells for large yaw angles from 60° to 90°. The number of cells for the fine mesh was about 28.2 million. The meshes were concentrated in a region of size 9.5 m in length, 2 m in width and 2.5 m in height around the motorbike through a refinement box in the SnappyHexMesh utility, as shown in Figure 3(c). The refinement box was used to increase the number of cells close to the motorbike and in the wake where large changes in the flow physics were expected. In addition, the mesh was refined in the direction of the wake flow through the use of three additional refinement boxes. For large yaw angles a refinement box was set in

the lee-side region of the motorbike, whereas for small yaw angles the refinement box included both the wake behind the motorbike and a part of the lee-side flow. A standard wall function was used in both the DDES and the RANS simulations. The mean wall normal resolution $y+$ value of the RANS and DDES simulations was approximately 100.

To obtain an accurate and stable solution in these simulations, a constant time step of 5×10^{-5} seconds was used to achieve a Courant-Friederich-Lewy (CFL) number below 1. In order to achieve the required criteria for the CFL number in the fine mesh, an even smaller time step of 1×10^{-5} seconds was used. Overall, a non-dimensional simulation time, $t^* = t\, U_{\text{eff}}/H$, of 55.5 was solved for, where t is the simulation time. Furthermore, the time-averaged flow was only acquired from the fully developed turbulent flow and averaged over $t^* = 18.5$. The visualization software ENSIGHT 9.2 was used to visualize the flow in this paper.

The simulations were performed using 16 processors in the Blue Birmingham Environment for Academic Research (Blue BEAR) computational facility. This facility has a Scientific Linux 6.6 operating system. The total wall time of the DDES simulations was approximately 900 hours, while the RANS simulations took approximately 90 hours.

5. Results and discussion

5.1. Mesh independence

Two different meshes – a coarse and fine mesh – are evaluated to investigate the grid independence of the simulations. For both meshes, the pressure coefficient around the body of the rider is calculated. The pressure coefficient, C_p, is defined as

$$C_P = \frac{\bar{p} - p_\infty}{\frac{1}{2}\rho\, U_{\text{eff}}^2}, \tag{5}$$

where $\bar{p}$ is the total time-averaged pressure, p_∞ is the free stream pressure, and ρ is the air density, defined as 1.205 kg/m^3. Figure 4 shows the surface C_p acting on the rider at a height of 1.12 m above the ground for a yaw angle of 15°. From Figure 4 it is clear that the DDES fine and coarse mesh yield similar results with respect to this parameter.

During the simulations the aerodynamic coefficients are calculated at each time step. The time-averaged drag force, C_D, side force, C_S, lift force, C_L, and rolling moment C_{Roll}, coefficients are defined as:

$$C_D = \frac{F_D}{0.5\, A\rho\, U_{\text{eff}}^2}, C_S = \frac{F_S}{0.5\, A\rho\, U_{\text{eff}}^2}, C_L = \frac{F_L}{0.5\, A\, \rho\, U_{\text{eff}}^2},$$
$$C_{\text{Roll}} = \frac{M_R}{0.5\, A\rho\, \text{L}\, U_{\text{eff}}^2}. \tag{6}$$

F_D, F_s, F_L and M_R are the drag force, side force, lift force and rolling moment, respectively. The characteristic area, A, is defined as 0.75 m^2, and L the wheel base of 1.5 m. The time-averaged values of the aerodynamic coefficients of the coarse and fine DDES simulations are averaged over the final 2.0×10^4 time steps ($t^* = 18.5$). In addition to the surface pressure, the aerodynamic force and moment coefficients of the different meshes are given in Table 1. It can be noted from Table 1 that the aerodynamic coefficients obtained from the fine mesh are in good agreement with the aerodynamic coefficients obtained from the coarse mesh. This indicates that the coarse mesh resolution is adequate to resolve the main flow features and thus no further refinement of the mesh is needed. All the results presented in the remaining sections of this paper are from the coarse mesh, unless otherwise stated.

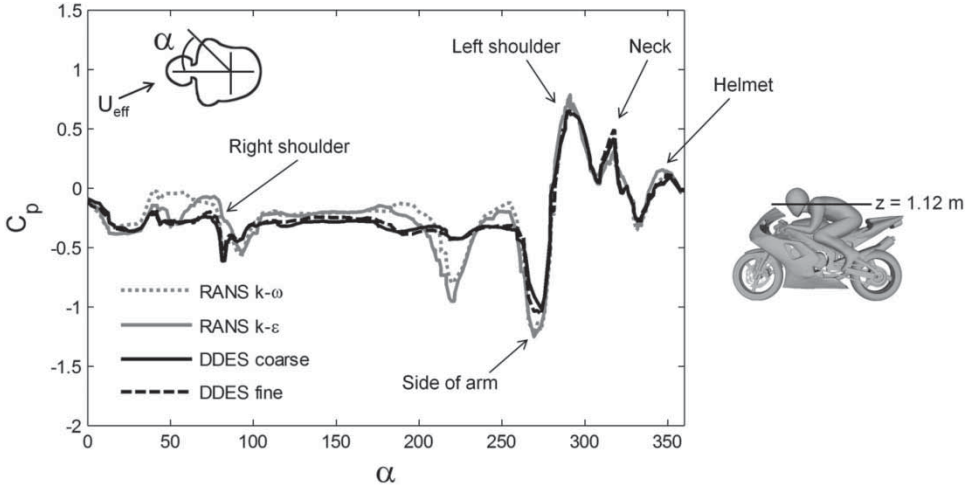

Figure 4. Pressure coefficient along a line on the surface of the rider parallel to the ground at a height of 1.12 m, at a yaw angle of 15° for all CFD approaches and the time-averaged DDES simulation results.

Table 1. Time-averaged aerodynamic coefficients for a coarse mesh and fine mesh of the DDES simulations at 15° yaw angle.

	Coarse	Fine
C_D	0.570	0.578
C_S	0.421	0.420
C_L	− 0.045	− 0.027
C_{Roll}	− 0.143	− 0.144
C_{Pitch}	0.218	0.215
C_{Yaw}	− 0.089	− 0.090

Table 2. Time-averaged aerodynamic coefficients for different yaw angles of the DDES simulations.

	$\beta = 15°$	$\beta = 30°$	$\beta = 60°$	$\beta = 90°$
C_D	0.570	0.560	0.288	− 0.148
C_S	0.421	1.050	1.838	2.084
C_L	− 0.045	0.030	0.317	0.412
C_{Roll}	− 0.143	− 0.389	− 0.690	− 0.761
C_{Pitch}	0.218	0.205	0.126	− 0.070
C_{Yaw}	− 0.089	− 0.178	− 0.149	0.024

5.2. Time-averaged flow

Figure 4 shows the peak pressure coefficients on both shoulders of the rider. The highest pressures are found at the windward (left) side of the rider, in particular around the shoulders ($\alpha = 290°$) and neck ($\alpha = 317°$). A low pressure area develops at the side of the left arm, indicating a region of flow separation. At the left side of the helmet and around the neck, high pressure regions are present. Figure 4 shows a quite similar behavior for the RANS and DDES results. However, a large negative surface pressure at $\alpha = 220°$ is visible in both RANS results which is not present in the DDES results. This low pressure area is located on the windward side, at the trunk of the rider's body between the arms and the legs. The disagreement is likely a result of the failure of the RANS models to accurately predict flow separation.

Figure 5 shows the streamlines around the motorbike at a height of 1.12 m above the ground. The main difference between the two CFD approaches (RANS and DDES) is the prediction of the location of the core of the recirculation region in the leeward side of the wake. Figure 5 shows that the core of the circulation region in the y-direction is located 0.035 m closer to the motorbike in both RANS simulations than that obtained with the time-averaged DDES results. The k-ε model showed the largest x-deviation from the location of the core in the DDES simulation. In the k-ε and k-ω models, the core was 0.087 m and 0.057 m closer to the motorbike in the x-direction, respectively.

The time-averaged aerodynamic coefficients of the DDES simulations for different crosswind angles are given in Table 2. For a super-sportive motorbike such as the one under investigation, C_D values between 0.45 and 0.6 are reported by Araki and Gotou (2001) of the Yamaha Motor Corporation. Ubertini and Desideri (2002) have reported an optimal drag area C_DA of around 0.3 m^2 for riders in an optimal aerodynamic position, e.g., 'lying' position. The DDES drag value at $\beta = 15°$ is about 0.57 (0.43 m^2), which is at the higher end of the range of the reported values at $\beta = 0°$. This can be justified by the fact that the drag can increase up to about 16% when increasing the yaw angle from 0–10° (Ubertini & Desideri, 2002).

The time-averaged force coefficients for the RANS and DDES simulations for the different yaw angles are shown in Figure 6. The main aerodynamic components that influence the stability of a motorbike and rider are the side force and the rolling and yawing moment coefficients. The C_S values increase from about 0.42 to 2.08 with increasing yaw angle, caused by the increasing stagnation pressure on the streamwise face and the reduction of the lee face pressure as a result of the recirculation region in the wake flow for large yaw angles. The side force and rolling moment coefficients appear to have an almost linear increase with respect to the yaw angle for values below $\beta \sim 60°$. Thereafter, the rate of change of these parameters decreases as a result of the flow structures occurring in the wake of the motorbike and rider. The peak side force and rolling moment coefficients are observed as occurring at a yaw angle of 90°, which possibly suggests this is

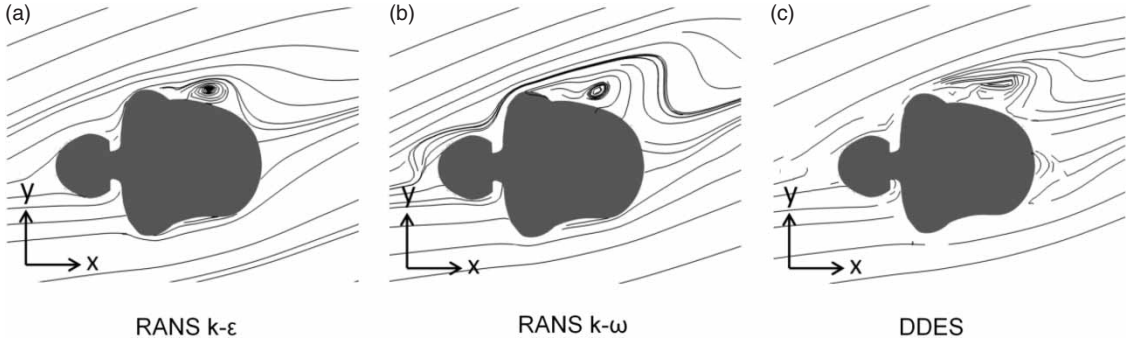

Figure 5. Streamlines around the motorbike in a plane at a height of 1.12 m from the ground of the different turbulence models.

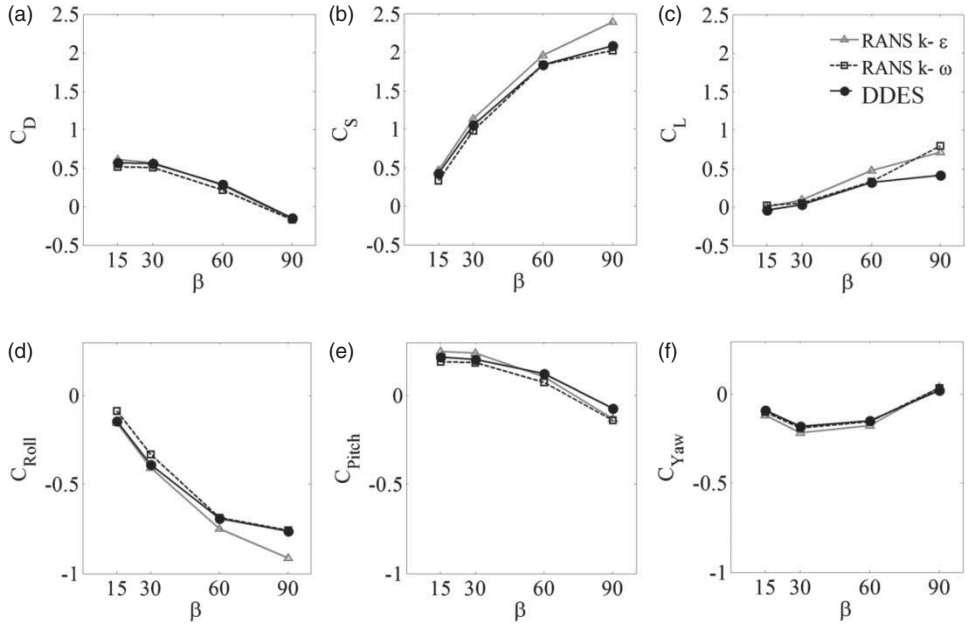

Figure 6. Aerodynamic force coefficients of the RANS and DDES simulations for different yaw angles.

the critical angle in terms of wind force and thus motorbike stability. The rolling moment coefficient values vary from -0.14 to -0.76 with increasing yaw angle. The C_D values decrease from about 0.57 to -0.15 with increasing yaw angle, caused by the increased side-wind velocity. The maximum drag force coefficient is observed for the small crosswind condition, i.e., $\beta = 15°$. The drag force coefficient decreases to nearly zero for $\beta = 90°$, i.e., pure crosswind conditions. The decrease in drag might affect the stability of the motorbike rider when subjected to a gust of wind. The dynamic nature of a gust of wind might result in sudden changes of the yaw angle and will, as this study shows, likely lead to a change in drag and might therefore affect the motorbike speed and stability. The decrease in drag coefficients under increasing yaw angles is also observed for other road vehicles, such as lorries (Baker, 1991; Hargreaves, Morvan, & Wright, 2006) and double decker buses (François, Delnero, Colman, Maranón, & Camocardi, 2009; Hemida & Krajnović, 2009b). The drag force coefficient is closely related to the pitching moment coefficient in which the moment coefficient gradually decreases with the yaw angle. Finally, the lift force coefficients are relatively small and tend to increase with increasing yaw angles. The maximum lift force coefficient is observed for the 90° crosswind condition.

It can be observed in Figure 6 that the RANS and DDES results are similar for the C_D. For large yaw angles, the RANS k-ε predicts 19% higher side forces than the two other approaches. It is commonly observed in external vehicle aerodynamics that the RANS k-ε model over-predicts the turbulent kinetic energy in a flow with strong anisotropic turbulence and non-equilibrium effects, such as the flow under investigation at large yaw angles (Makowski & Kim, 2000). Similarly, there are discrepancies in the lift forces between the RANS and DDES approach at large yaw angles. This can be related to the failure of RANS approaches to accurately predict the separation and reattachment regions. Therefore, the results of the DDES simulations have been used to explore the flow around the motorbike in the time-averaged and instantaneous flow unless otherwise explicitly stated.

Figure 7 shows the pressure contour lines on the motorbike and rider at different crosswind yaw angles. It can be clearly seen that at $\beta = 15°$ (Figure 7(a)), high pressure areas and stagnation points exist on the helmet (s1), windshield (s2) and shoulder (s3). These stagnation points appear to move towards the side of the body as the yaw angle increases. At large yaw angles ($> 30°$), stagnation points s2 and s3 disappear and new stagnation points emerge at the side of the rider (s4) and at the side of the motorbike (s5). However, the stagnation point (s1) remains on the head with an increase in yaw angle.

In Figure 8, the iso-surface of the time-averaged pressure coefficient around the motorbike is shown for yaw angles of 15°, 30°, 60° and 90° with C_p values of -0.29, -0.36, -0.5 and -0.64, respectively. For a 15° yaw angle (Figure 8(a)), low pressure regions predominantly exist at the back of the rider. With increasing yaw angle, low pressure areas develop at the leeward side and front of the motorbike, in particular at the windshield. These low pressure regions contribute significantly to the aerodynamic forces.

Figures 9 and 10 show the time-averaged streamlines for different crosswind yaw angles on two different planes parallel to the ground at heights of $z/H = 0.8$ and $z/H = 0.4$, respectively. The vortex cores of the main

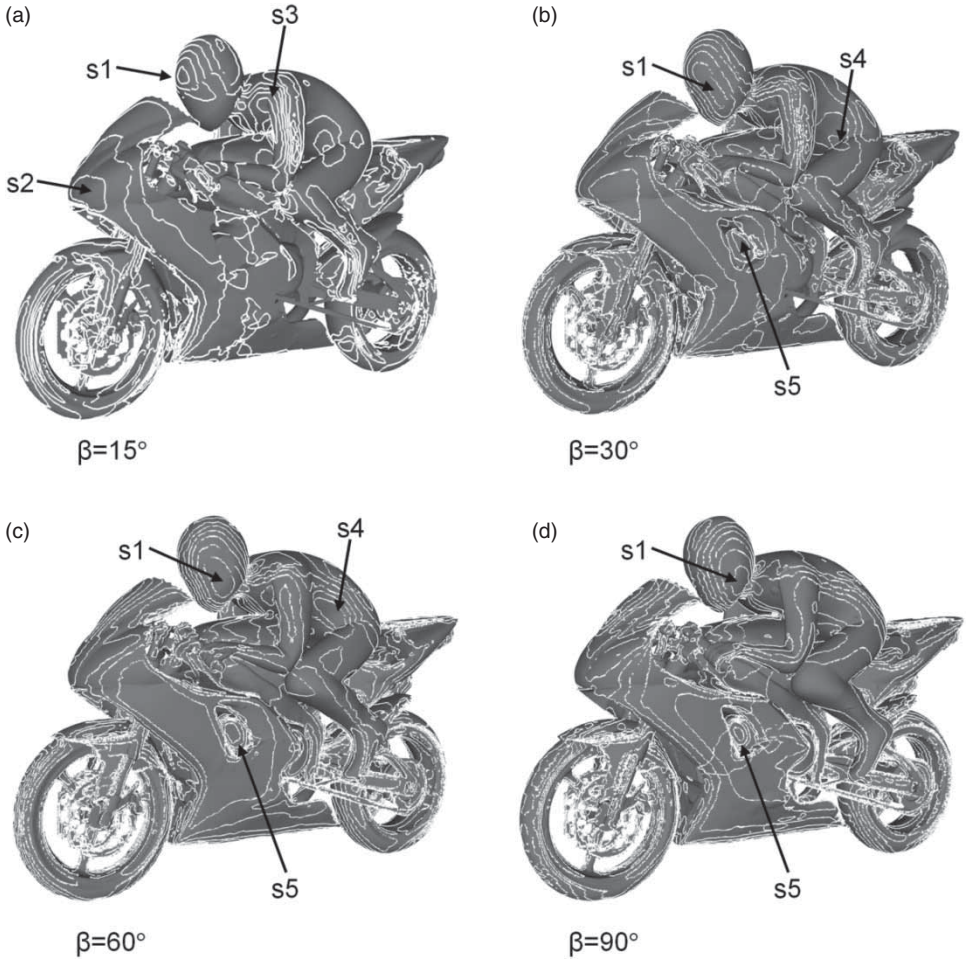

Figure 7. Pressure contour lines of the DDES simulations on motorbike and rider at different yaw angles. Stagnation points are shown on the head (s1), windshield (s2), left shoulder (s3), thigh (s4) and motorbike (s5).

flow are also shown. Differences in flow behavior can be observed for the two planes. For the plane at $z/H = 0.8$ (Figure 9), at small crosswind yaw angles ($\beta = 15$–$30°$), recirculation areas are found close to the side of the rider (v1–v2). At larger yaw angles ($> 30°$), the flow becomes more turbulent, resulting in an increase in the number of vortex cores (v3–v6). These vortex cores also move further away from the rider as a result of increased vortex shedding and flow separation. This is paired with the increase of the size of the wake. For the plane at $z/H = 0.4$ in Figure 10, recirculation areas are mainly found at the back of the motorbike for $\beta = 15$–$30°$ (v7–v8). At yaw angles $> 30°$, there are large circulation areas at the leeward side of the motorbike (v9–v13), whereas at $\beta = 60°$ the main vortex cores v9–v11 are centrally located in the wake, and at $\beta = 90°$ the vortex cores v12 and v13 move more to the edges of the wake. This is predominantly caused by the flow streams around the sides of the wheels of the motorbike.

The time-averaged flow features are visualized using the vortex core technique (Banks & Singer, 1994), which is based on the Eigen-analysis algorithm. The computed vortex cores of the time-averaged flow around the motorbike at different crosswind yaw angles are shown in Figure 11. The recirculation regions shown in the time-averaged streamlines of the motorbike in Figures 9 and 10 are also found in the vortex cores. The large number of vortex core lines reveals the complex turbulent flow around the motorbike. The flow becomes more turbulent with increasing yaw angle, which is caused by the increased number of bluff bodies seen by the upcoming flow. The low pressure regions at the back and head of the rider shown in Figure 8 are also present as vortex cores v14 and v15 respectively. Similarly, around the windshield a low pressure region develops which corresponds with vortex core v16 for yaw angles $> 30°$.

5.3. *Transient flow*

The second invariant of the velocity gradient tensor, Q, is used to visualize the instantaneous flow field and to determine the positions of the vortex cores, where Q is

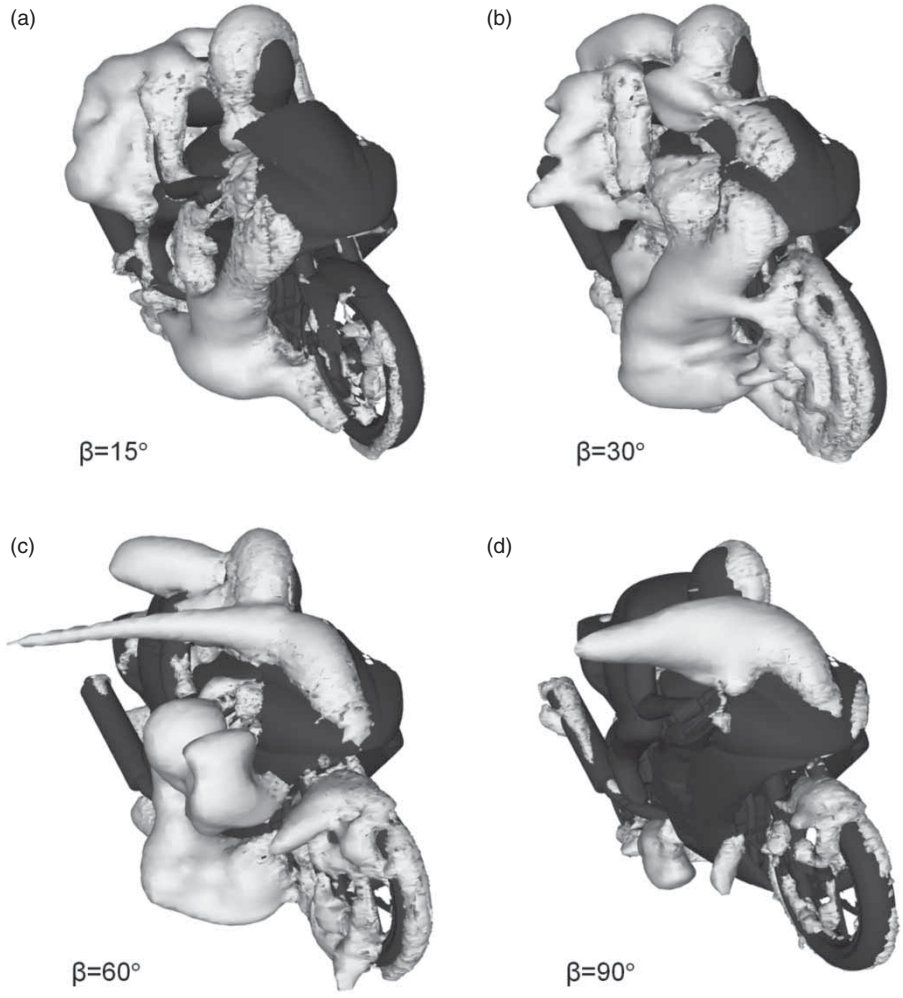

Figure 8. Iso-surface around motorbike of the DDES turbulence model for the time-averaged flow at different yaw angles. The coefficient of pressure has been set to: (a) $C_p = -0.29$, (b) $C_p = -0.36$, (c) $C_p = -0.5$, and (d) $C_p = -0.64$.

defined as

$$Q = -\frac{1}{2}\, u_{ij}\; u_{ji}\;. \tag{7}$$

Figure 12 shows the temporal development of the vortex structures at different crosswind angles for $Q = 8 \times 10^3$. Many vortices are born at the entire leeward side of the motorbike and rider surface. These vortices are convected downstream by the crosswind flow. The vortex structures are stretched over a larger wake distance from the motorbike with increasing yaw angles. However, at a yaw angle of 90°, the wake vortices remain closer to the motorbike and are smaller in size. The attachment and detachment of the flow from the body contribute to high-frequency modes in the aerodynamic forces.

The time histories of the force coefficients at different yaw angles are shown Figure 13. Large variations of the force coefficients are found, which are caused by the instability and movement of the wake vortices that are disturbing the instantaneous motorbike surface pressure. For large yaw angles, the variations are increasingly significant compared to small yaw angles, which are caused by strong vortex shedding. The largest force coefficient variations are found in the lift forces.

The time histories of the force coefficients are used to reveal the frequencies of the flow around the motorbike. The power spectral densities (PSDs) of the time-varying signals are calculated to evaluate the distribution of the power of the signal over the frequencies. The PSDs are calculated by multiplying the Fourier transform of the time-varying signal by the conjugate of the Fourier transform. Figure 14 shows the PSDs plotted versus the Strouhal number, *St*, for different yaw angles and force coefficients. The Strouhal number is defined as

$$St = \frac{f\;H}{U_{\text{eff}}} \tag{8}$$

where f is the frequency and H is the characteristic length, defined as the height of the motorbike from the ground. An

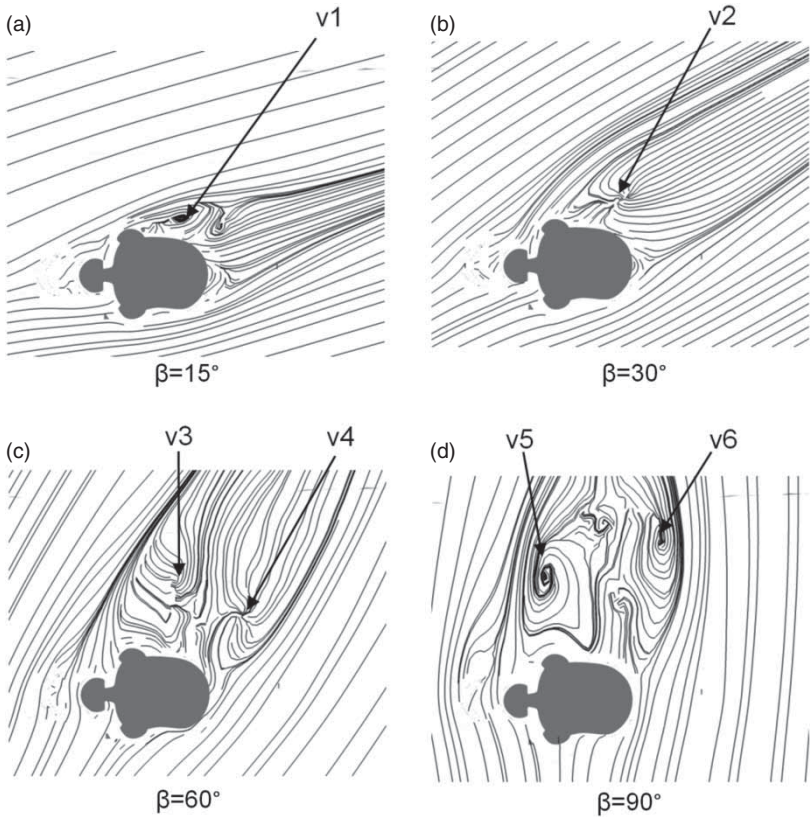

Figure 9. Time-averaged streamlines and the positions of the main vortex cores of the DDES simulations on a surface parallel to the ground at $z/H = 0.8$ and at different crosswind yaw angles.

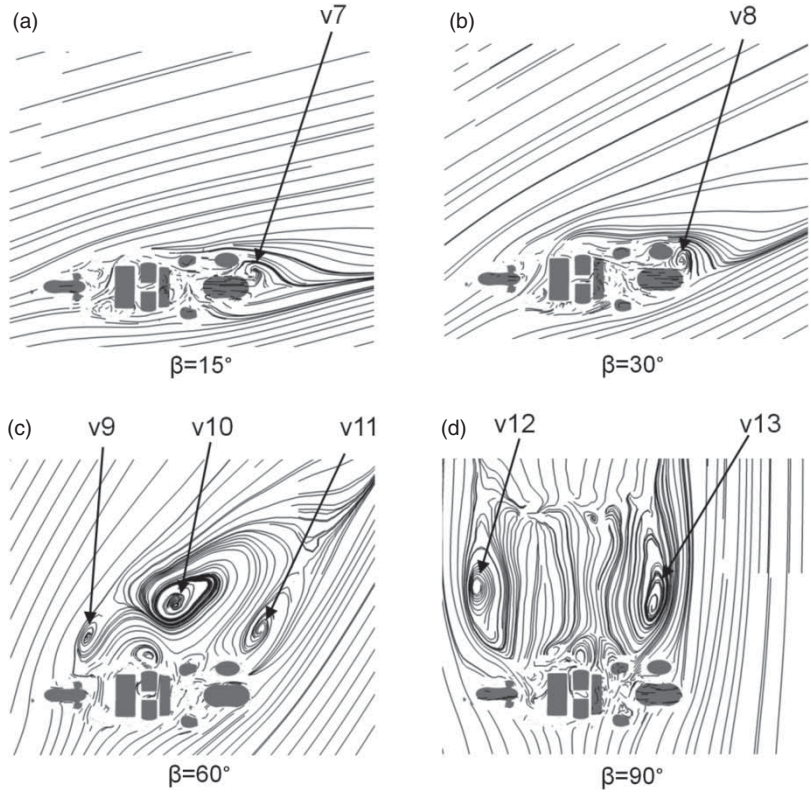

Figure 10. Time-averaged streamlines and the positions of the main vortex cores of the DDES simulations on a surface parallel to the ground at $z/H = 0.4$ and at different crosswind yaw angles.

overview of the Strouhal numbers of the dominant peaks is given in Table 3.

In all PSDs of the force coefficients, the energy of the dominant peaks increases at higher yaw angles (Figure 14). Predominately low-frequency peaks are found in the PSDs. These low-frequency peaks account for vortex shedding in the wake of the motorbike. Furthermore, high-frequency peaks in the drag force coefficient are mainly found in the 60° and 90° crosswind yaw angle situations. This can be explained by the attachment and detachment of the small flow structures on the surface of the motorbike and to the shear layer instabilities. The dominant low-frequency peaks in the PSD of the C_D lie in the Strouhal number range $0.2 < St < 1.7$. For the C_S, the dominant frequencies are found in the range $0.1 < St < 2.1$, while for the C_L in the range $0.1 < St < 1.2$. The energy of the dominant frequency in the lift force coefficient is up to seven times higher than that of the other force coefficients.

Some of the dominant low frequency peaks appear multiple times at different yaw angles. The dominant peak,

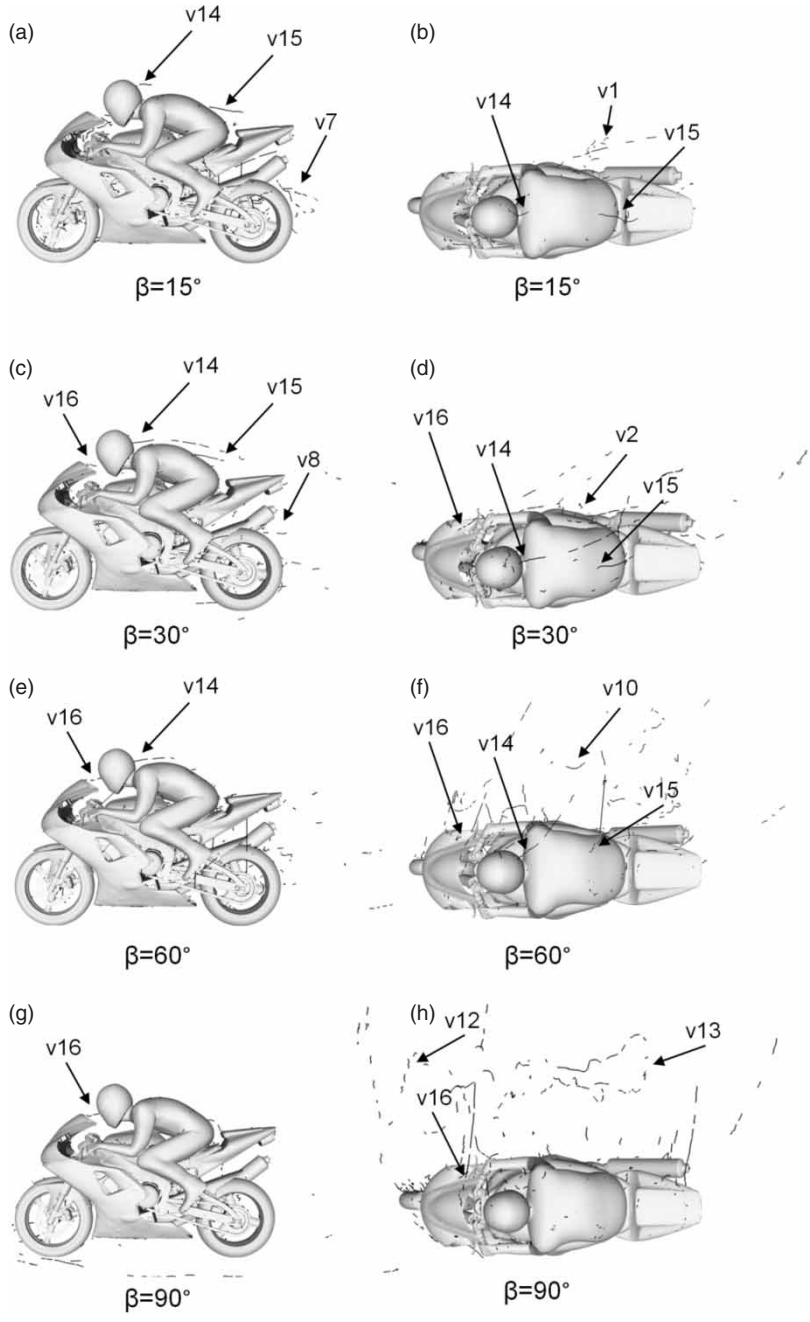

Figure 11. Vortex cores of the time-averaged velocity field of the DDES simulations around the motorbike at different crosswind yaw angles and different orthogonal views: side view and top view.

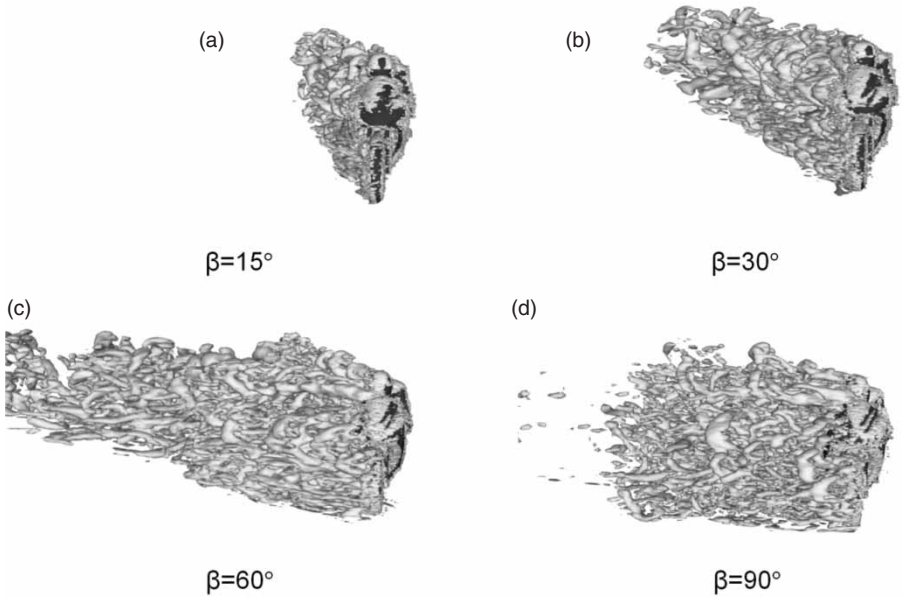

Figure 12. Instantaneous iso-surface of the velocity gradient tensor, Q, around the motorbike at different crosswind angles of the DDES simulations, for $Q = 8 \times 10^3$.

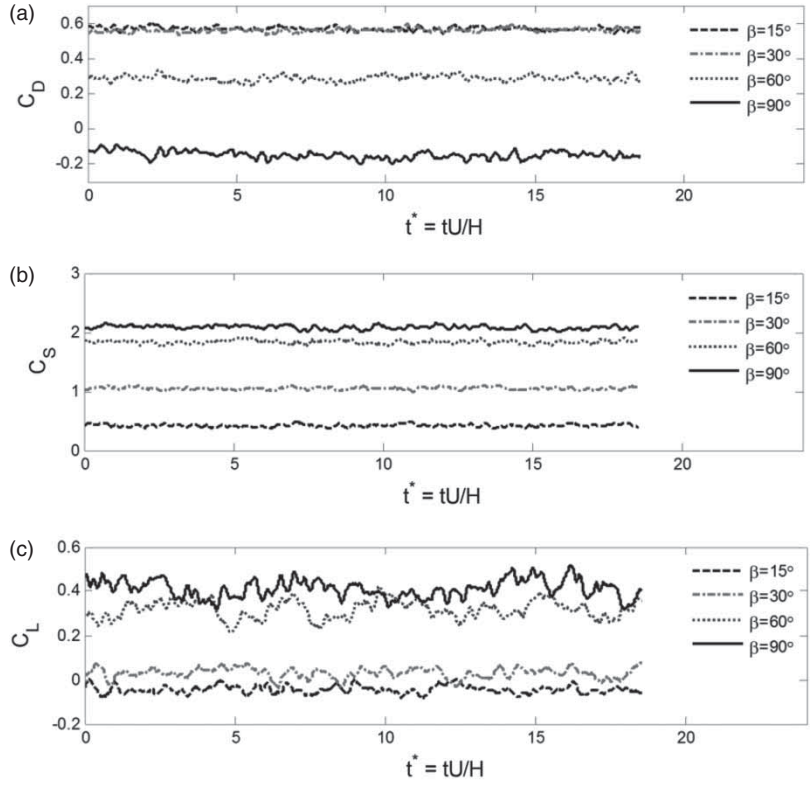

Figure 13. Time histories of the force coefficients on the motorbike at different yaw angles obtained from the DDES simulations: (a) drag force coefficient, C_D, (b) side force coefficient, C_S, and (c) lift force coefficient, C_L.

$St = 0.162$, in the PSD of the C_S at $\beta = 30^\circ$ and $\beta = 60^\circ$ can also found as the dominant peak in the PSD of the C_L at $\beta = 60^\circ$ and $\beta = 90^\circ$. This is also the case for the dominant peak $St = 0.216$ in the PSD of the C_D at $\beta = 60^\circ$, which appears in the PSD of the C_L at $\beta = 30^\circ$. Another common frequency is $St = 0.270$, which appears as a dominant peak in the C_D at $\beta = 90^\circ$ and in the C_L at yaw angles 15° and 60°, respectively.

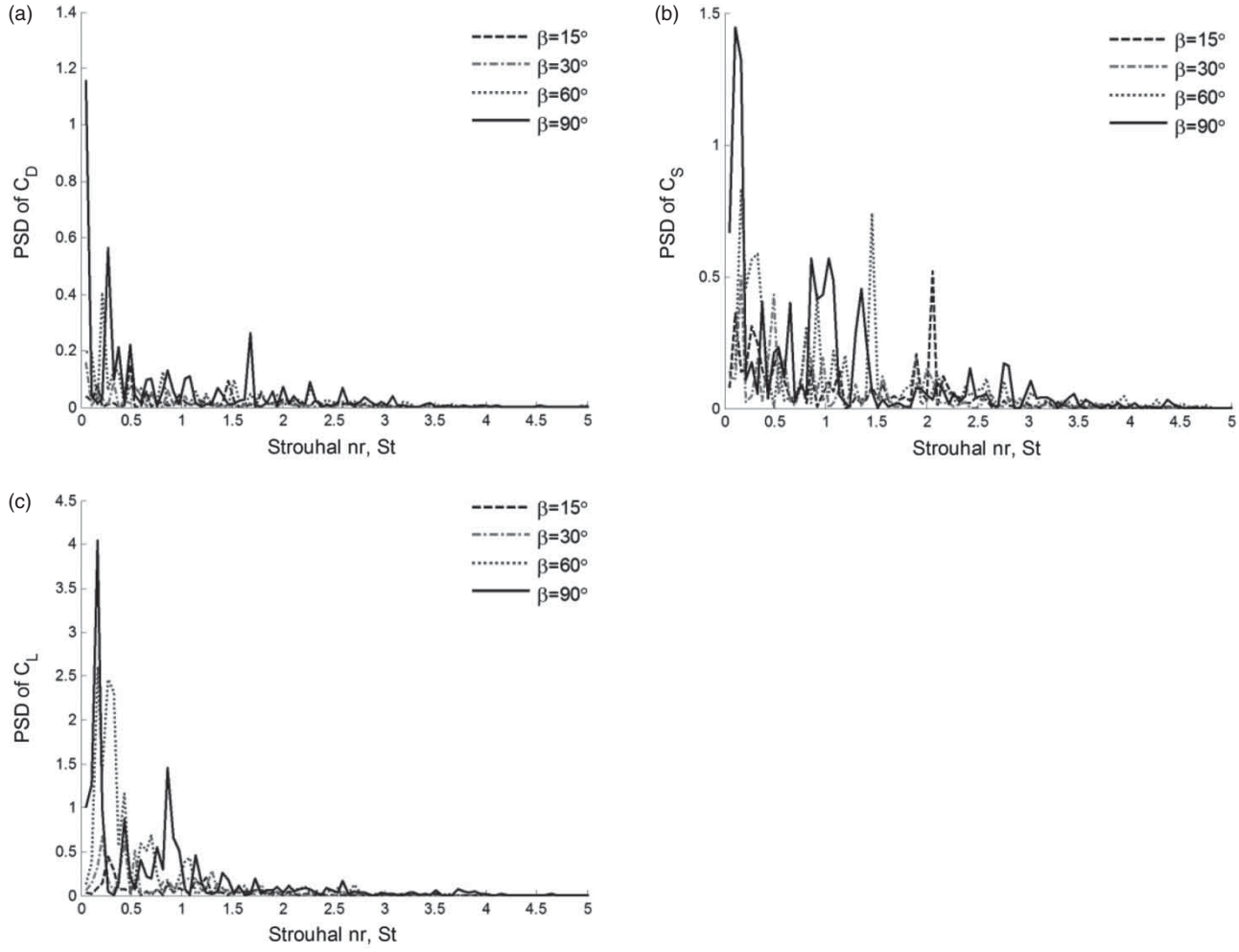

Figure 14. Strouhal number versus power spectral density of the time-varying aerodynamic forces for different yaw angles obtained from the DDES simulations: (a) PSD of drag force, (b) PSD of side force, and (c) PSD of lift force.

Table 3. Strouhal numbers of the two dominant peaks in the force coefficient data for different yaw angles of the DDES simulations.

	$\beta = 15°$	$\beta = 30°$	$\beta = 60°$	$\beta = 90°$
C_D	0.486	0.324	0.216	0.270
	1.458	0.540	0.810	1.674
C_S	2.052	0.162	0.162	0.108
	0.108	0.486	1.458	0.864
C_L	0.270	0.216	0.162	0.162
	1.242	0.432	0.270	0.864

6. Conclusion

The work of this paper represents the first numerical study investigating the time-averaged and instantaneous flow around a motorbike subjected to crosswinds. DDES and RANS simulations were performed on the flow around a motorbike subjected to crosswind with yaw angles ranging from 15° to 90°. Results showed that the time-averaged aerodynamic coefficients of the RANS are in reasonably good agreement with those of the DDES simulations. However, differences are observed in the location and size of the recirculation regions and associated surface pressures. The rolling moments, side forces and lift forces increase with the yaw angle, while the drag forces decrease. The peak side forces are almost four times higher than the peak drag forces. The DDES results showed that high surface pressures are predominantly found on the helmet and motorbike for almost all yaw angles. Main vortex cores are found behind the helmet, at the back of the rider and at the windshield, reflecting the highly turbulent flow at these regions. In particular behind the windshield, strong vortex shading takes place for yaw angles $> 15°$.The vortex shedding is found to be stronger at higher yaw angles. From the results it could be suggested that optimization of the design of the motorbike, with focus on the windshield, could help to improve the safety of motorbike riders in crosswinds. The CFD results have provided valuable data for other numerical and experimental work. It is recommended that future work should attempt to reveal the effects of gusts on motorbike stability, since it is hypothesized that these

are likely to play a significant role in determining safety criteria.

Disclosure statement

No potential conflict of interest was reported by the authors.

References

Angeletti, M., Sclafani, L., Bella, G., & Ubertini, S. (2003). The role of cfd on the aerodynamic investigation of motorcycles. *SAE Technical Paper 2003-01-0997*. doi:10.4271/2003-01-0997

Araki, Y., & Gotou, K. (2001). Development of aerodynamic characteristics for motorcycles using scale model wind tunnel. *SAE Technical Paper 2001-01-1851*. doi:10.4271/2001-01-1851

Baker, C., Cheli, F., Orellano, A., Paradot, N., Proppe, C., & Rocchi, D. (2009). Cross-wind effects on road and rail vehicles. *Vehicle System Dynamics*, *47*(8), 983–1022. doi:10.1080/00423110903078794

Baker, C. (1991). Ground vehicles in high cross winds part I: Steady aerodynamic forces. *Journal of Fluids and Structures*, *5*, 69–90.

Banks, D. C., & Singer, B. A. (1994). Vortex tubes in turbulent flows – Identification, representation, reconstruction *Institute for Computer Applications in Science and Engineering*. Hampton: NASA Langley Research Center.

Bridges, P., & Russell, J. B. (1987). The effect of topboxes on motorcycle stability. *Vehicle System Dynamics*, *16*(5–6), 345–354.

Carr, A. (2011, 12 August 2013). Fatal motorcycle crash, wind gust causes Sherman wreck, from http://www.post-journal.com/page/content.detail/id/583501/Fatal-Motorcycle-Crash.html?nav = 5192

Cheli, F., Belforte, P., Melzi, S., Sabbioni, E., & Tomasini, G. (2006). Numerical-experimental approach for evaluating cross-wind aerodynamic effects on heavy vehicles. *Vehicle System Dynamics*, *44*, 791–804. doi:10.1080/00423110600886689

Cheli, F., Bocciolone, M., Pezzola, M., & Leo, E. (2006, 4–7 July 2006). *Numerical and experimental approaches to investigate the stability of a motorcycle vehicle.* Paper presented at the Proceedings of the 8th Biennial Conference on Engineering Systems Design and Analysis, Turin, Italy.

Chu, L.-M., Chang, M.-H., Hsu, H.-C., Chien, W.-T., & Liu, C.-H. (2008). Simulation and experimental measurement of flow field within four-stroke motorcycle engines. *Journal of the Chinese Society of Mechanical Engineers*, *29*(2), 149–158.

Cooper, K. R. (1983). The effect of handlebar fairings on motorcycle aerodynamics. *SAE Technical Paper*, *830156*. doi:10.4271/830156

Donell, S. (2010, 18 April). Wind blamed in fatal motorcycle accident, *NBC Washington*. Retrieved from http://www.nbcwashington.com/news/local/Weather-Blamed-in-Freak-Fatal-Motorcycle-Accident-91433499.html

François, D., Delnero, J., Colman, J., Maranón, D. L. J., & Camocardi, M. (2009). Experimental determination of Stationary Aerodynamics loads on a double deck Bus. 11th Americas Conference on Wind Engineering, San Juan, Puerto Rico.

Gauger, W. (2013). Fatal motorcycle crash in Waupaca Co. Retrieved 14 August 2013, from http://www.fox11online.com/dpp/news/local/fox_cities/fatal-motorcycle-crash-in-waupaca-co

Gentilli, R., Zanforlin, S., & Frigo, S. (2006, 4–7 July 2006). *Numerical and experimental analysis on a small GDI, stratified charge, motorcycle engine.* Paper presented at the Proceedings of the 8th Biennial Conference on Engineering Systems Design and Analysis, Turin, Italy.

Guilmineau, E., & Chometon, F. (2009). Effect of side wind on a simplified car model: Experimental and numerical analysis. *Journal of Fluids Engineering*, *131*(2), 021104.

Hargreaves, D. M., Morvan, H. P., & Wright, N. G. (2006). CFD modeling of high-sided vehicles in cross-winds. *The Fourth International Symposium on Computational Wind Engineering (CWE2006)*. Yokohama, Japan.

Hemida, H., & Baker, C. (2010). Large-eddy simulation of the flow around a freight wagon subjected to a crosswind. *Computers & Fluids*, *39*(10), 1944–1956. doi:10.1016/j.compfluid.2010.06.026

Hemida, H., & Krajnović, S. (2009a). Exploring flow structures around a simplified ICE2 train subjected to a 30° side wind using LES. *Engineering Applications of Computational Fluid Mechanics*, *3*(1), 28–41. doi:10.1080/19942060.2009.11015252

Hemida, H., & Krajnović, S. (2009b). Transient simulation of the aerodynamic response of a double-deck bus in gusty winds. *Journal of Fluids Engineering*, *131*(3), 031101.

Issa, R. I. (1986). Solution of the implicitly discretised fluid flow equations by operator-splitting. *Journal of Computational Physics*, *62*, 40–65.

Launder, B. E., & Spalding, D. B. (1974). The numerical computation of turbulent flows. *Computer Methods in Applied Mechanics and Engineering*, *3*(2), 269–289. doi:http://dx.doi.org/10.1016/0045-7825(74)90029-2

Makowski, F. T., & Kim, S.-E. (2000). Advances in external-aero simulation of ground vehicles using the steady RANS equations. *SAE Technical Paper*, *2000-01-0484*. doi:10.4271/2000-01-0484

Menter, F. R. (1992). Improved two-equation *k*-omega turbulence models for aerodynamic flows. *NASA-TM-103975, NASA-TM-103975*.

Sakagawa, K., Yoshitake, H., & Ihara, E. (2005). Computational fluid dynamics for design of motorcycles (Numerical analysis of coolant flow and aerodynamics). *SEA Technical Paper*, *2005-32-0033*. doi:10.4271/2005-32-0033

Scibor-Rylski, A. J., & Sykes, D. M. (1984). *Road vehicle aerodynamics* (2nd ed.). Plymouth: Pentech Press.

Shuhei, A. (2006). Fuel cell powered motorcycles. *Journal of the Society of Automotive Engineers of Japan*, *60*(1), 90–93.

Spalart, P. R., Deck, S., Shur, M. L., Squires, K. D., Strelets, M. K., & Travin, A. (2006). A new version of detached-eddy simulation, resistant to ambiguous grid densities. *Theoretical and Computational Fluid Dynamics*, *20*, 181–195.

Sterling, M., Quinn, A. D., Hargreaves, D. M., Cheli, F., Sabbioni, E., Tomasini, G., . . . Morvan, H. (2010). A comparison of different methods to evaluate the wind induced forces on a high sided lorry. *Journal of Wind Engineering and Industrial Aerodynamics*, *98*(1), 10–20. doi:10.1016/j.jweia.2009.08.008

Takahashi, Y., Kurakawa, Y., Sugita, H., Ishima, T., & Obokata, T. (2009). CFD analysis of airflow around the rider of a motorcycle for rider comfort improvement. *SAE Technical paper*, *2009–01-1155*. doi:10.4271/2009-01-1155

Tsubokura, M., Nakashima, T., Kitayama, M., Ikawa, Y., Doh, D. H., & Kobayashi, T. (2010). Large eddy simulation on the unsteady aerodynamic response of a road vehicle in transient crosswinds. *International Journal of Heat*

and Fluid Flow, *31*(6), 1075–1086. doi:10.1016/j.ijheatfluidflow.2010.05.008

Ubertini, S., & Desideri, U. (2002). Aerodynamic investigation of a scooter in the university of perugia wind tunnel facility. *2002-01-0254*. Retrieved from http://dx.doi.org/10.4271/2002-01-0254 doi:10.4271/2002-01-0254

Wang, B., Xu, Y. L., Zhu, L. D., Cao, S.-Y., & Li, Y.-L. (2013). Determination of aerodynamic forces on stationary/moving vehicle-bridge deck system under crosswinds using computational fluid dynamics. *Engineering Applications of Computational Fluid Mechanics*, *7*(3), 355–368.

Wang, B., Xu, Y. L., Zhu, L. D., & Li, Y.-L. (2014). Crosswind effect studies on road vehicle passing by bridge tower using computational fluid dynamics. *Engineering Applications of Computational Fluid Mechanics*, *8*(3), 330–344.

Watanabe, T., Okubo, T., Iwasa, M., & Aoki, H. (2003). Establishment of an aerodynamic simulation system for motorcycle and its application. *Jsae Review*, *24*(2), 231–233. doi:10.1016/S0389-4304(03)00003-1

Yamaha. (2009). YZF-R1: History 1998–2010, from http://www.yamaha-motor.eu/designcafe/en/about-bikes/supersport/index.aspx?view = article&id = 442650